

# MICROSCOPIC PREDICTIONS FOR CLUSTER-DECAYS

Mihail MIREA<sup>a</sup>, Aureliu SANDULESCU<sup>b,c</sup>, Doru Sabin DELION<sup>a,b</sup>

<sup>a</sup>*Horia Hulubei National Institute for Physics and Nuclear Engineering, P.O. Box MG-6,  
Bucharest, Romania*

<sup>b</sup>*Bioterra university, 81 Gârlei str., Bucharest, Romania*

<sup>c</sup>*Institute for Advanced Studies in Physics, Bucharest, Romania*

---

## Abstract

The decay dynamical path is determined within the macroscopic-microscopic model for the emission of  $^{24}\text{Ne}$  from  $^{232}\text{U}$ . The nuclear shape parametrization is characterized five degrees of freedom. The single particle energies and the nucleon wave functions are obtained within the superasymmetric Woods-Saxon two center shell model. It turns out that the cluster decay follows a potential magic valley, starting from the ground state of the parent and reaching a configuration of two touching nuclei at scission. A small pocket in the potential barrier is evidenced, as a result of large shell effects in the nascent fragments. The half-life is computed by using several approaches for the effective mass. It is shown that the inertia within by the gaussian overlap approach gives the closest values to the experimental ones. Half-lives for different cluster decays are predicted. The theoretical values are compared to various phenomenological estimates.

*Keywords:* Woods-Saxon two center shell model, Cluster decay, Cold fission.

---

## 1. Introduction

The cluster decay was predicted in 80's [1, 2, 3, 4, 5, 6] and experimentally evidenced in 1984 [8, 9, 10, 11]. Since then, the spontaneous emission of heavy fragments was intensively investigated. An unified phenomenological approach of the cluster radioactivity, cold fission and alpha decay as well as many body theories were used [7]. Later on, a fine structure in cluster emission was also predicted [12]. Energy spectrum measurements concerning

$^{14}\text{C}$  emission from  $^{223}\text{Ra}$  [13, 14] revealed a fine structure with an intense branch to the excited state of  $^{209}\text{Pb}$ . The best agreement between experiment and theory was obtained by considering the cluster decay as a fission process [15, 16], treated within the macroscopic-microscopic model. Only the experimental hindrance factors were reasonably reproduced. The difference between the theoretical and experimental absolute half-lives was subject of many orders of magnitude.

In this work, our aim is to develop a macroscopic-microscopic approach to treat in a unitary manner the cluster decay and the fission process, in order to reproduce theoretically the half-lives. For this purpose, a fission like theory will be used to determine the best sequence of nuclear shapes for the cluster decay. In this context, the minimal action principle will be used. Two ingredients are needed: the deformation energy of the disintegrating system and the nuclear inertia. The half-life of the  $^{24}\text{Ne}$  emission from  $^{234}\text{U}$  is determined within the WKB approximation and compared to the experimental values. Such an elaborated study of the fission dynamics in a wide range of mass asymmetries could help us to better understand the underlying physics and to provide an unitary treatment of cluster decay and fission. In this respect, the calculations evidenced a pocket shape of the potential barrier in the path towards scission. This pocket has a different nature with respect to the double potential barrier associated to fission. In fission, the second well is obtained as an isomeric state of the parent nucleus. From this isomeric state, the single particle levels are strongly rearranged to give the asymptotic configuration of two separated fragments. This rearrangement is evidenced by the strong positive shell effects of the second barrier. *In cluster decay the evidenced pocket belongs to a magic valley that leads directly to the cluster emission. This valley belongs to a mass asymmetry consistent with the formation of the  $^{208}\text{Pb}$ .* Predictions for other decay modes from  $^{234}\text{U}$  are also performed.

## 2. Model

### 2.1. Fission trajectory

The calculation addresses  $^{24}\text{Ne}$  cluster emission from  $^{232}\text{U}$ . The microscopic-macroscopic model [17] is exploited dynamically, by determining the least action trajectory. The dynamical analysis of a fissioning nucleus requires at least the knowledge of the deformation energy and the effective mass. For simplicity, in the macroscopic-microscopic model one assumes that these

quantities depend upon the shape coordinates. Thus, in our analysis, the basic ingredient is the nuclear shape parametrization. The nuclear shape parametrization used is given by two ellipsoids of different sizes smoothly joined by a third surface obtained by rotating a circle around the symmetry axis. Five degrees of freedom characterize this nuclear shape parametrization: the elongation, given by the inter-nuclear distance  $R = z_2 - z_1$  between the centers of the ellipsoids, the two deformations of the nascent fragments denoted by their eccentricities  $\epsilon_i = [1 - (b_i/a_i)^2]^{1/2}$  ( $i=1,2$ ), the mass asymmetry given by the ratio of major semi-axis  $\eta = a_2/a_1$  and the necking parameter related to the curvature of the intermediate surface  $C = s/R_3$ . The quantity  $C$  is used for swollen shapes in the median region, while  $R_3$  is used for necked shapes. The meaning of the geometric symbols can be understood by inspecting Fig. 1. A single nucleus and two separated fragments are allowed configurations. The determination of the fission trajectory can be obtained through a minimization of the action integral in our five-dimensional configuration space, starting with the ground state of the system and ending at the exit point of the barrier or in the scission configuration. For fission, such calculations were already realized for Th, U [18, 19] and Cf[20].

The probability  $P$  of a given channel in a fission process is ruled by an exponential factor within the WKB approximation [21].

$$P = \exp \left\{ -\frac{2}{\hbar} \int_{R_i}^{R_f} \sqrt{2(V(R, C, \epsilon_1, \epsilon_2, \eta)B \left( R, C, \epsilon_1, \epsilon_2, \eta, \frac{\partial C}{\partial R}, \frac{\partial \epsilon_1}{\partial R}, \frac{\partial \epsilon_2}{\partial R}, \frac{\partial \eta}{\partial R} \right) dR} \right\} \quad (1)$$

The exponent of the above relation gives the classical action integral of a fixed energy along a trajectory in our multidimensional configuration space. In the present work, this energy is considered as the ground state energy of the parent nucleus. In fission, the trajectory connects the ground state configuration  $R_i$  to the exit point of the barrier  $R_f$ . In the cluster decay case, the minimization has to be performed up the configuration of two touching nuclei, denoted  $R_t$ . To this purpose, two ingredients are required: the deformation energy  $V$  and the tensor of the effective mass  $B$ .

## 2.2. Deformation energy

The deformation energy  $V$  was obtained by summing the liquid drop energy  $E_{LDM}$  with the shell and the pairing corrections  $\delta E$ :

$$V = E_{LDM} + \delta E . \quad (2)$$

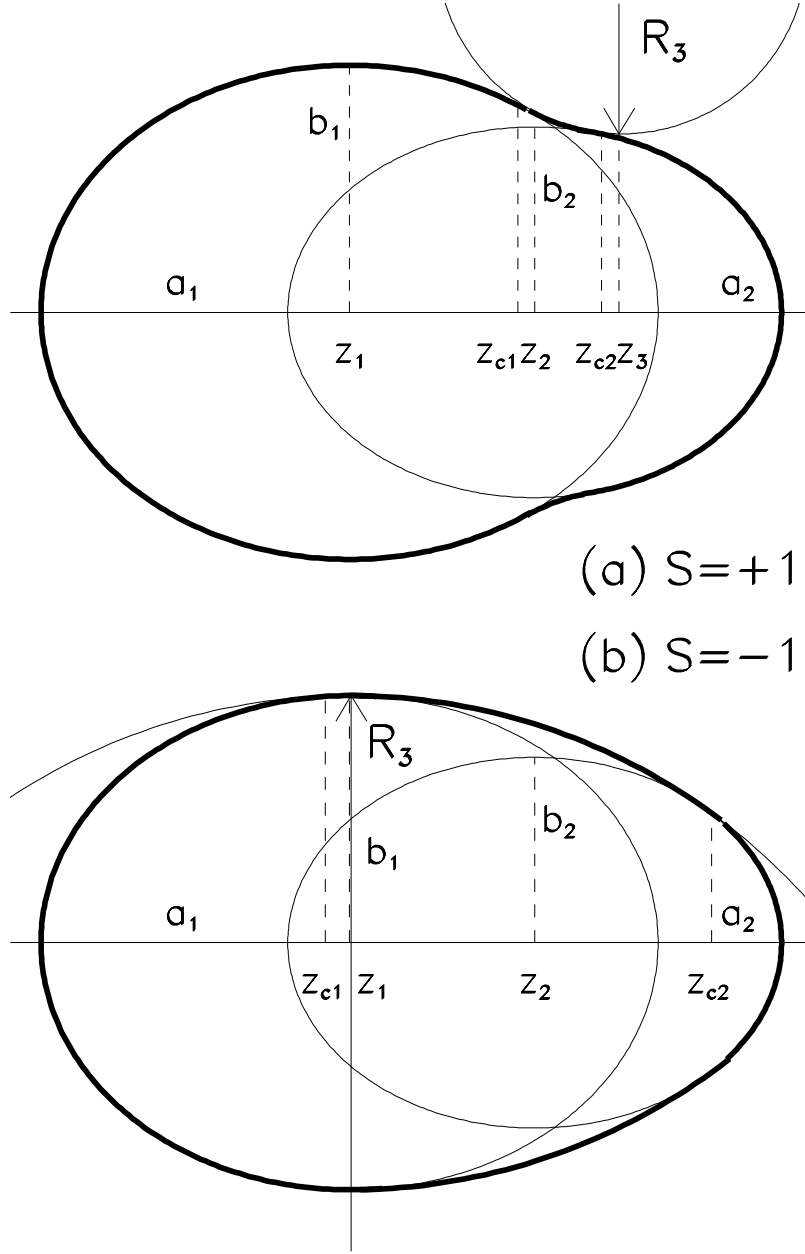


Figure 1: Nuclear shape parametrization.

The macroscopic energy  $E_{LDM}$  is obtained in the framework of the Yukawa

plus - exponential model [22] extended for binary systems with different charge densities [23] as detailed in Ref. [24]:

$$E_{LDM} = E_n + E_C + \Delta E_C + E_V + E_W + E_{A_0} , \quad (3)$$

where

$$E_n = -\frac{a_2}{8\pi^2 r_0^2 a^4} \int_V \int_V \left( \frac{r_{12}}{a} - 2 \right) \frac{\exp\left(-\frac{r_{12}}{a}\right)}{\frac{r_{12}}{a}} d^3 r_1 d^3 r_2 , \quad (4)$$

is the nuclear term,

$$E_C = \frac{1}{2} \int_{-\infty}^{\infty} \int_{-\infty}^{\infty} \frac{\rho_e(r_1) \rho_e(r_2)}{r_{12}} d^3 r_1 d^3 r_2 , \quad (5)$$

is the Coulomb energy for a constant electric density  $\rho_e$ ,

$$\Delta E_C = -\frac{\rho^2}{2} \int_V \int_V \frac{1}{r_{12}} \exp^{-r_{12}/a} \left( 1 + \frac{r_{12}}{2a} \right) d^3 r_1 d^3 r_2 , \quad (6)$$

is a diffuseness correction to the Coulomb potential as described in Ref. [22], and  $E_V$  is the volume energy. In the finite range droplet model [25] there are also several terms that are not deformation dependent. The most important are the Wigner term  $E_W$  and the  $A^0$  energy  $E_{A_0}$ . Both were added in the potential energy. These terms don't have a shape dependence and were neglected in previous investigations. In the following, these terms vanish in the overlapping region up to an elongation close to the scission configuration  $R_t$ . They are supposed to reach linearly their final value for a distance larger than 2 fm between the surfaces of the separated fragments, where the nuclear forces vanish. In the previous definitions  $\rho_e$  are charge densities and  $r_{12} = |\vec{r}_1 - \vec{r}_2|$ . The charge densities are considered constant inside the volume of the nucleus in Eq. (5) and zero outside. Another degree of freedom has to be introduced here, namely the charge asymmetry. Usually [23], one considers that  $\rho_e$  is charge density of the parent nucleus for an elongation smaller than  $0.7R_t$ , where  $R_t$  is the elongation characterizing the configuration of two touching fragments, and varies linearly up to the final values of the two nascent nuclei at scission. This charge equilibration procedure is described in Ref. [26].

### 2.3. Shell effects

The shell effects  $\delta E$  are obtained as a sum between the shell  $\delta U$  and pairing  $\delta P$  corrections. In this context the Strutinsky procedure was used. These corrections represent the varying part of the total binding energy caused by the intrinsic structure. In calculating the pairing effect, constant values of the pairing matrix elements are computed separately for the parent and the two fragments. A renormalization procedure [21] in the BCS theory that depends on the energy level distribution and a smoothed gap distribution is used to obtain the values of the pairing matrix elements associated to each fragment issued in the the reaction. To have a smooth transition between the shell effects that characterize the parent nucleus to those associated to the configuration given by two separated nuclei a simple approximation was used. The shell and pairing effects are computed by using the whole level scheme from the spherical nuclear shape up to the elongations  $R_{int}=8.5$  fm. Beyond  $R_{fin}=12$  fm the two fragments are separated and there are no ambiguities in determining the wave functions located in the potential well of the daughter or in that of the emitted nucleus by using the procedure described in Ref. [27]. Thus, beyond  $R_{fin}$  the shell and pairing corrections are determined separately for each nucleus by using the appropriate level schemes for the parent and the daughter nuclei. Between these two configurations located at  $R_{int}$  and  $R_{fin}$ , we used a gradual interpolation of the type:

$$u_k = u_k + (u_k^{fin} - u_k)(R - R_{int})/(R_{fin} - R_{int}) \quad (7)$$

$$v_k = v_k + (v_k^{fin} - v_k)(R - R_{int})/(R_{fin} - R_{int}) , \quad (8)$$

where  $u_k$  and  $v_k$  are the vacancy and occupation amplitudes, respectively, calculated for the whole level scheme, while  $u_k^{fin}$  and  $v_k^{fin}$  are their values computed separately for each nascent fragment at the elongation  $R_{fin}$ .

### 2.4. Effective mass

The deformation energy is a function of the collective parameters, giving the generalized forces acting on the nuclear shape. For a complete description of the fission process, it is also necessary to know how the nucleus reacts to these generalized forces. This information is contained in the effective mass of the system [21]. The most used approach to calculate the inertia is the cranking model. Recently, the cranking model was generalized by taking into account the intrinsic excitation produced during the fission process itself [28]. In our investigation, three different approximations to describe the inertia are

used. First of all, for the determination of the fission trajectory, the mass parameters are evaluated microscopically within the cranking model. In order to evaluate the half-life, two other approximations are used: the Gaussian Overlap Approximation (GOA) and the diabatic Cranking formula by using Time Dependent Pairing Equations (CTDPE). Relations concerning these models are given in the Appendix.

### 2.5. Microscopic potential

To calculate the inertia and the shell effects, we need a microscopic potential. The microscopic potential has to be consistent with our nuclear shape parametrization. The simplest way to define the mean field is to use a semi-phenomenological Woods-Saxon potential. In order to take into account nuclear deformations going over to separate shapes, a two-center shell model with a Woods-Saxon potential was recently developed [16]. The mean field potential is defined by the relation:

$$V_0(\rho, z) = \frac{V_c}{1 + \exp \left[ \frac{\Delta(\rho, z)}{a} \right]}, \quad (9)$$

where  $\Delta(\rho, z)$  is the distance between a point  $(\rho, z)$  and the nuclear surface. This distance is measured only along the normal direction on the surface and it is negative if the point is located in the interior of the nucleus.  $V_c$  is the depth of the potential, while  $a$  is the diffuseness parameter. In our work, the depth is  $V_c = V_{0c}[1 \pm \kappa(N_0 - Z_0)/(N_0 + Z_0)]$  with plus sign for protons and minus sign for neutrons,  $V_{0c} = 51$  MeV,  $a=0.67$  fm,  $\kappa=0.67$ . Here,  $A_0$ ,  $N_0$  and  $Z_0$  represent the mass number, the neutron number and the charge number of the parent, respectively. This parametrization, usually referred as the Blomqvist-Wahlborn one, is adopted because it provides the same constant radius  $r_0$  for the mean field and the pairing field. It ensures a consistency of the shapes of the two fields at hyperdeformations, i.e., two tangent ellipsoids. The Hamiltonian is obtained by adding the spin-orbit and the Coulomb terms to the Woods-Saxon potential. The eigenvalues are obtained by diagonalizing the Hamiltonian in the semi-symmetric harmonic two center basis [29, 30]. In this work, the maximal principal quantum number is  $N_{max} = 14$ . The two center Woods-Saxon model will be used to compute shell and pairing corrections together with inertia. The two center shell model represents a valuable instrument to investigate the role of individual orbitals for the treatment of a wide variety of superasymmetric

disintegration processes, pertaining to cluster- and alpha-decays [15, 31, 32] or superheavy elements [33, 34].

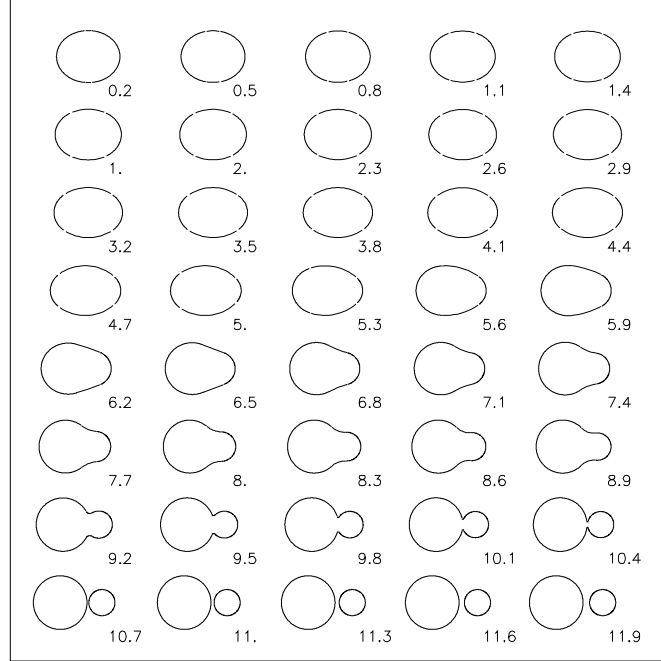


Figure 2: Family of shapes along the minimal action trajectory for cluster decay. The elongation  $R$  in fm is marked for each shape.

### 3. Results and discussion

#### 3.1. Action integral minimization

It is not possible to directly minimize the functional (1), due to the large computing time determining the values of the potential energies and of the effective masses. Thus, in the relevant configuration space, a small number of potential energies and inertia are computed and their interpolated values are used in the minimization procedure. First of all, a grid of 691 200 deformation values was fixed in our five-dimensional configuration space: 20 values of  $R$



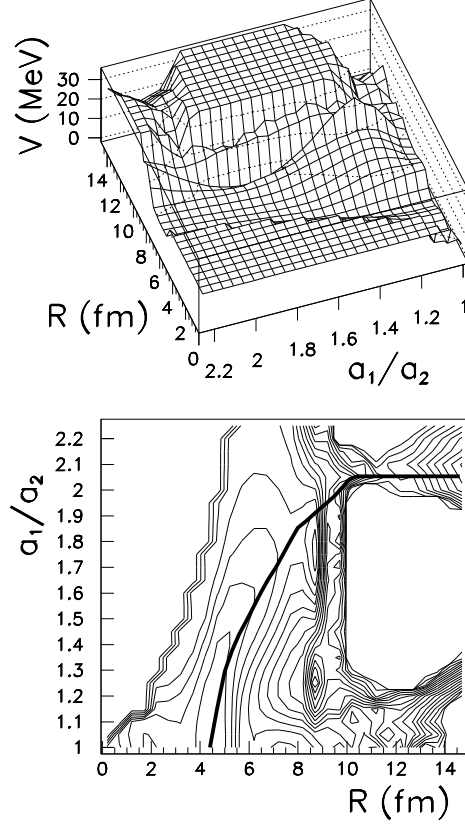


Figure 3: Upper part: potential energy surface  $V$  as function of the elongation  $R$  and the mass asymmetry  $\eta = a_1/a_2$ . Lower part. contour plot of the potential energy surface. The step between two equipotential curves is 2 MeV. The variations of the coordinates  $\epsilon_1$ ,  $\epsilon_2$ , and  $C$  follow the least action path as function of  $R$ . The least action trajectory is plotted within a thick curve.

between 0 fm and the scission point, 8 values of eccentricities  $\epsilon_i$  between 0 and 0.75, 15 values of the ratio  $\eta = a_1/a_2$  in the interval 1 and 3 and 32 values for  $C$  between 0.11 and 0.20 fm<sup>-1</sup>, (5 values for  $R_3$  between 0 and 4 fm are also added). The deformation energy and the elements of the inertia tensor were computed in these selected points. In this way, the pertinent region in the configuration space including the possible fission trajectories between the ground state and the scission configuration  $R_t$  was spanned. The quantities of interest in this selected region were obtained by interpolating the calculated masses and the energies. The trajectory emerges by minimizing numerically

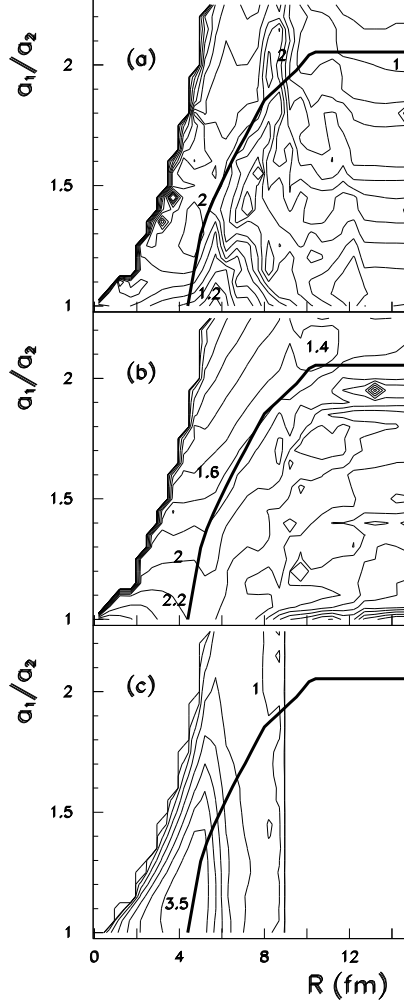


Figure 4: The diagonal components of the main effective masses divided by the reduced mass  $\mu$  of the  $^{24}\text{Ne}$  emission. Upper panel:  $B_R/\mu$  (dimensionless with step between two curves of 0.2). Middle panel:  $\log(B_\eta/\mu)$  (the dimension of  $B_\eta/\mu$  is  $\text{fm}^2$  and the step between two curves is 0.2). Lower panel:  $\log(B_C/\mu)$  (the dimension of  $B_C/\mu$  is  $\text{fm}^4$  and the step between two curves is 0.5). The least action trajectory is plotted by a thick curve. Some values of the mass parameter are marked on the plot.

the action functional, according to Ref. [36] used to describe the fission process.

The family of nuclear shapes for the cluster decay along the least action trajectory are plotted in Fig. 2. The supersymmetric fission trajectory, as

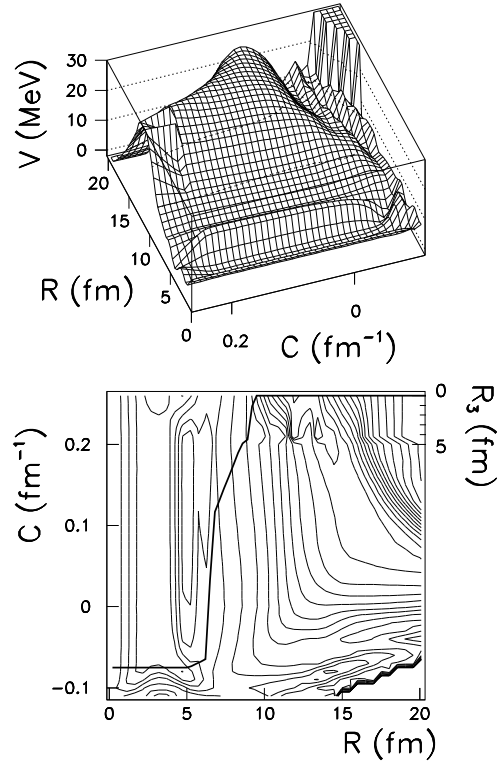


Figure 5: Same as Fig. 3 for a representation in the  $C$  and  $R$  generalized coordinates. For  $C$  greater than  $0.2 \text{ fm}^{-1}$  one uses the right scale for  $R_3 = 1/C$ . The step between two equipotential lines is 2 MeV.

well as the landscapes of the deformation energies and the main components of the tensor of effective masses, are displayed in Figs. 3, 4, 5 and 6, respectively. In Fig. 3, the potential energy surface is represented as function of the mass asymmetry parameter  $\eta = a_1/a_2$  and the elongation  $R$ . The dependencies of all generalized coordinates as function of  $R$  follow the variation obtained along the minimal action trajectory. The ground state of the parent nucleus is located at an elongation  $R=4.6 \text{ fm}$  with a mass asymmetry  $\eta \approx 1$ . The ratio  $a_1/a_2$  abruptly changes when the nucleus starts to deform, i.e., when the elongation increases. A compatible with the final mass asymmetry value is very soon obtained. It is clearly evidenced that the nuclear system follows a well behaved valley in the potential energy surface up to the scission configuration located at  $R_t \approx 10 \text{ fm}$ . The scission configuration is approximatively

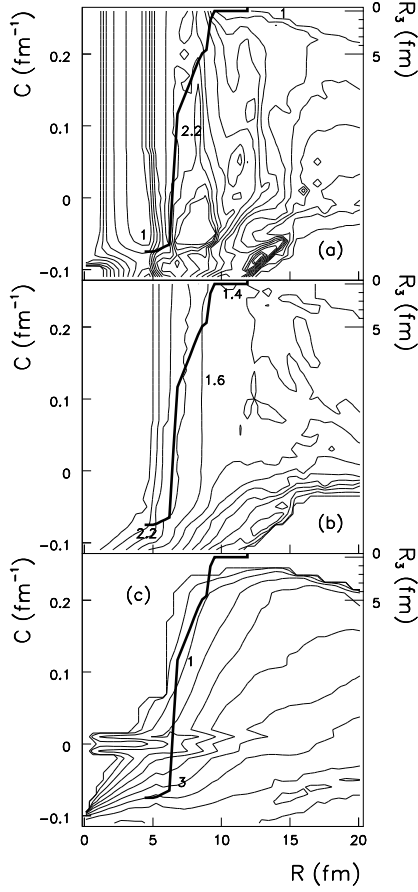


Figure 6: Same as Fig. 4 for a representation in the  $C$  (or  $R_3$ ) and  $R$  generalized coordinates.

described by two tangent spherical fragments. It is interesting to stress that in the case of the fission phenomena, the situation is very different. The behavior for fission is displayed for  $a_1/a_2 \approx 1$ -1.2 fm, where two fragments of comparable sized are formed. It can be seen in Fig. 2 that a double barrier occurs. The nucleus, initially in the ground state, is fissioning by penetrating a first barrier located at  $R=6.5$  fm and reaches a second well at  $R=7$  fm. The situation is completely different for the cluster decay [35]: as mentioned the system follows an energy valley in the deformation energy. When the elongation is larger than  $R_t$ , the valley in the potential energy surface is extended in the external region for the system  $^{208}\text{Pb}+^{24}\text{Ne}$ . Keeping in mind that the trajectory is determined by the interplay between the deformation

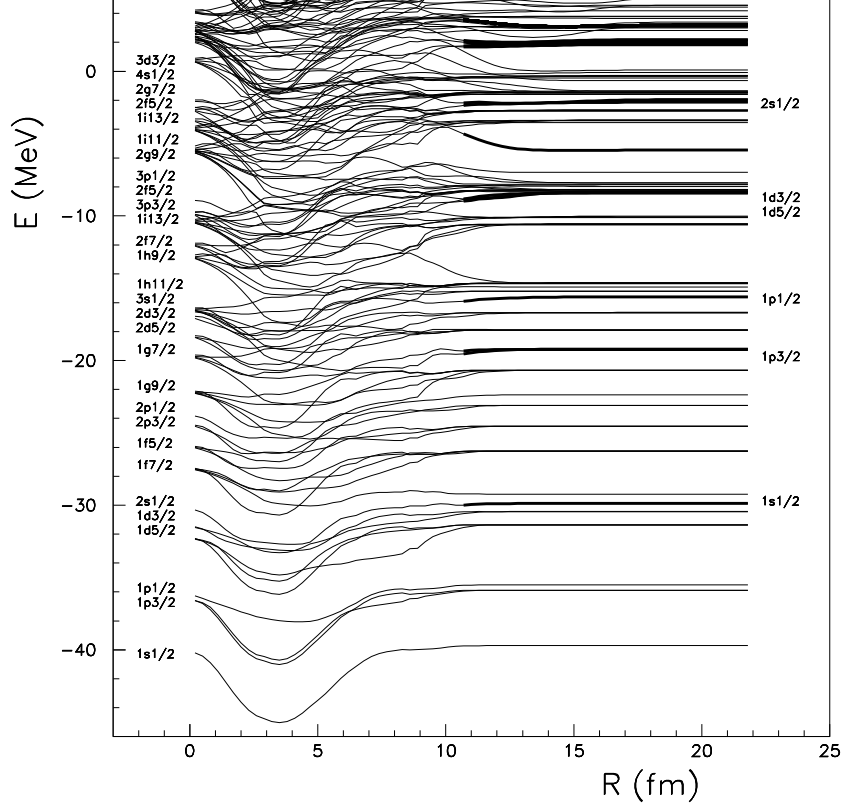


Figure 7: Neutron level diagram for  $^{24}\text{Ne}$  cluster decay from  $^{232}\text{U}$  with respect to the elongation  $R$ .

energy and the effective mass, we plotted in Fig. 4 the diagonal components  $B_{RR}$ ,  $B_{\eta\eta}$  and  $B_{CC}$  of the inertia tensor as function of  $a_1/a_2$  and  $C$ . The trajectory has a smooth variations following the contour lines trying to avoid large values of the effective masses. A sudden variation of the trajectory is not allowed because any rapid variation is translated into an increase of the mass. This effect can be understood by appealing to the formula (A.2). The inertia along a path has a strong dependence on the derivatives of the generalized coordinates. This behavior confirms the aspects discussed in Ref. [37] in the case of the Werner-Wheeler approach. For each mass asymmetry at scission, the effective mass  $B_{RR}$  reaches a value close to the reduced mass.

In Fig. 5, the deformation energy is displayed in the plane  $(C, R)$ . The ground state is located at  $R=4.6$  fm and has a necking parameter  $C=0.075$

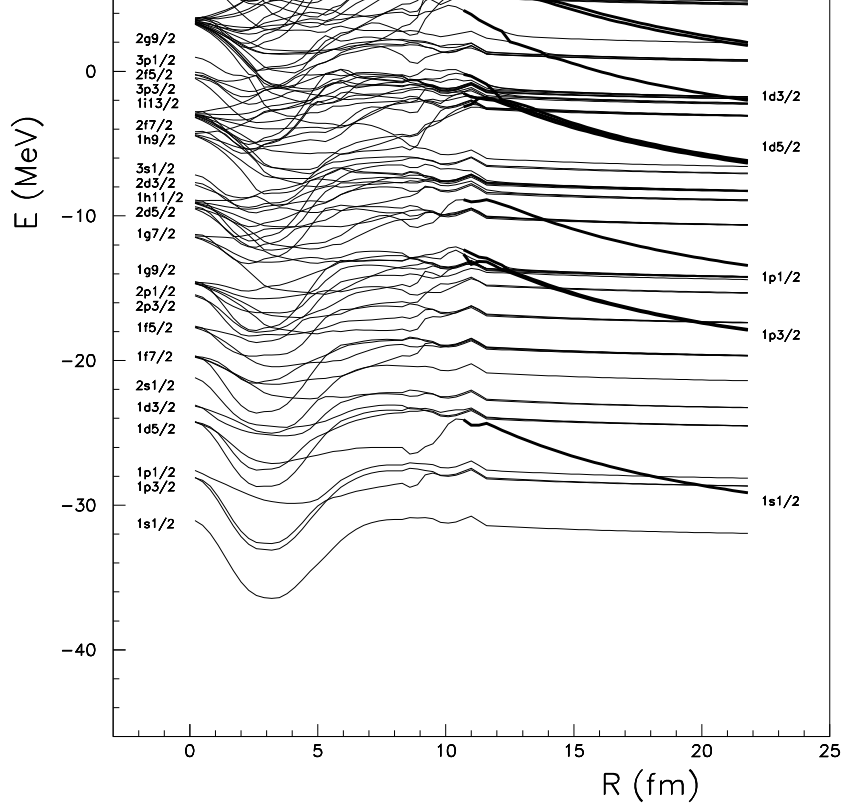


Figure 8: Proton level diagram for  $^{24}\text{Ne}$  cluster decay from  $^{234}\text{U}$  with respect to the elongation  $R$ .

$\text{fm}^{-1}$ . So, in the ground state the shapes are swollen. These swollen shapes are preserved up to  $R=6$  fm. From this value, the necking parameter starts to vary abruptly and the shapes become very necked producing the rupture at  $R_t \approx 10$  fm. At scission, the configuration of nearly two touching nuclei is obtained. The variations of the generalized parameters corresponds to an increase of the total inertia. The variation of the effective mass is directly connected to this evolution of the nuclear system as it can be seen from Fig. 6, where the main components of the effective mass are plotted. The values of  $B_{CC}$  are large for small or negatives values of  $C$ . Thus, in order to have a minimal value of the action integral the nucleus has to rapidly escape from this region. Notice that the values of the effective mass in the scission region are smaller for  $C \rightarrow \infty$  (or  $R_3 = 0$  fm). Let us mention that  $B_{\eta\eta}$  decreases

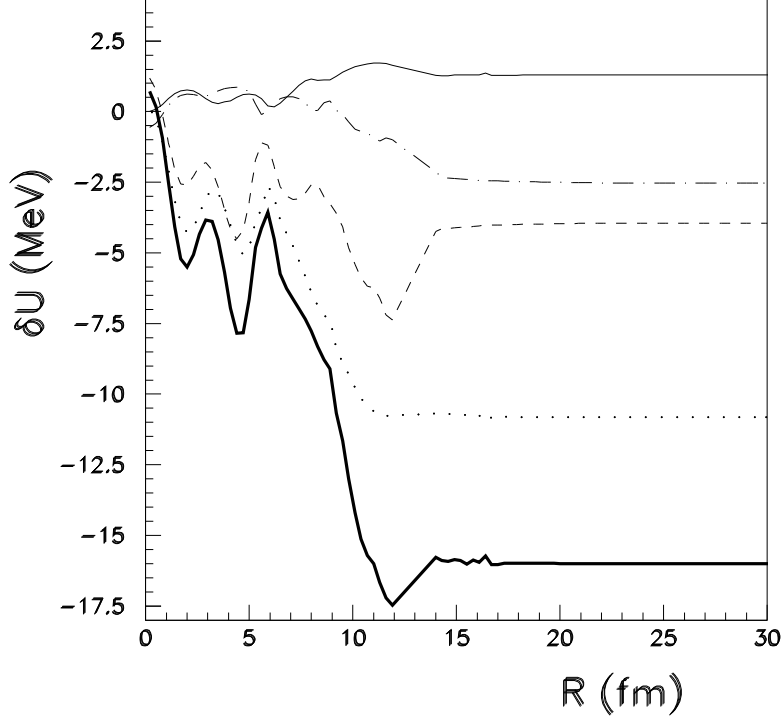


Figure 9: Shell effects  $\delta U$  as function of the elongation  $R$ : the thick full curve denotes the total shell effect  $\delta E$ , the thin dashed line gives the proton shell effect, the thin dot dashed line represents the proton pairing contribution, the thin dotted line is the neutron shell effect, while the full thin curve denotes the neutron pairing contribution.

with mass asymmetry and  $B_{CC}$  vanishes after scission.

### 3.2. Level diagrams

The neutron and proton single-particle diagrams are calculated along the minimal action trajectory, from the ground state of the parent nucleus and beyond the formation of two separated fragments. These level schemes are plotted in Figs. 7 and 8 for neutrons and protons, respectively. In Fig. 7, at  $R \approx 0$ , the parent nucleus is considered spherical. For small deformations, the system evolves in a way similar to a Nilsson diagram for prolate deformations. In the left side of Fig. 7, the orbitals of the parent nucleus (considered spherical) are labeled by their spectroscopic notations. The levels of the

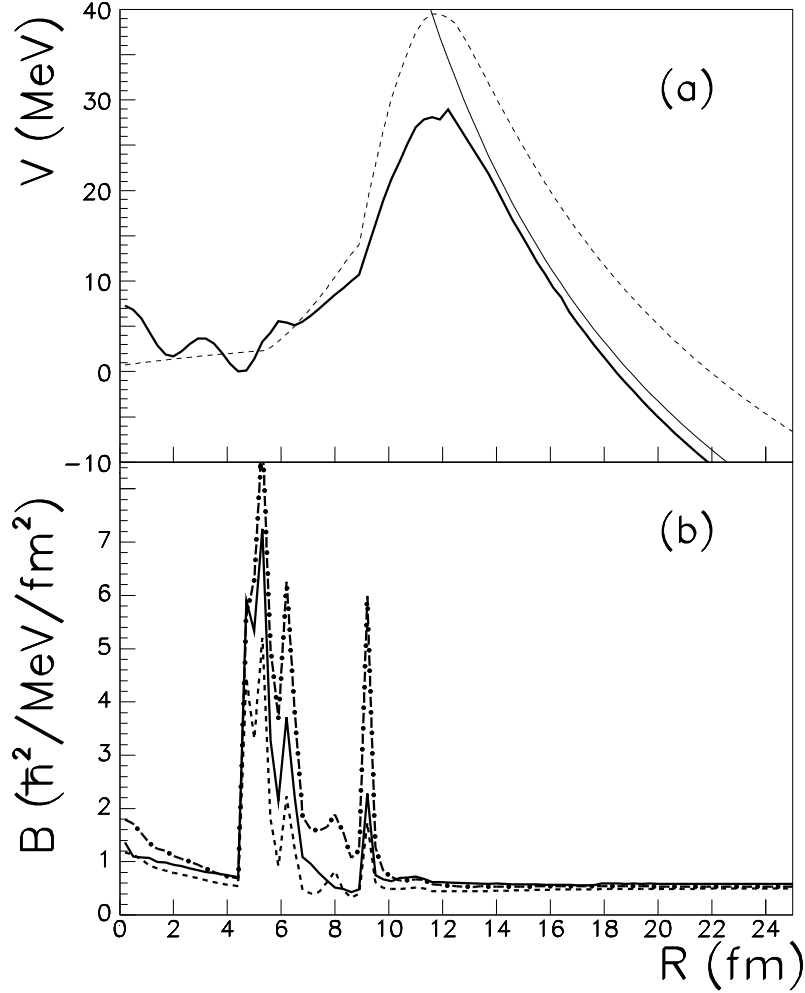


Figure 10: (a) The macroscopic-microscopic potential barrier  $V$  for the  $^{24}\text{Ne}$  emission as a function of the elongation  $R$  is plotted by a thick curve. The thin curve represent the Coulomb energy  $Z_1 Z_2 e^2 / R - Q$  relative to the experimental  $Q$ -value of the process. The dashed line represents the barrier given by the liquid drop model, without shell effects. (b) The effective mass along the minimal action trajectory calculated within the semi-adiabatic model (full curve), the GOA (dashed curve) and the cranking model (dot-dashed curve).

emitted fragment can be identified and we plotted them by thick lines. Both fragments are spherical after scission and their levels are bunched in shells. The levels of the light fragment are labeled by their spectroscopic notations.



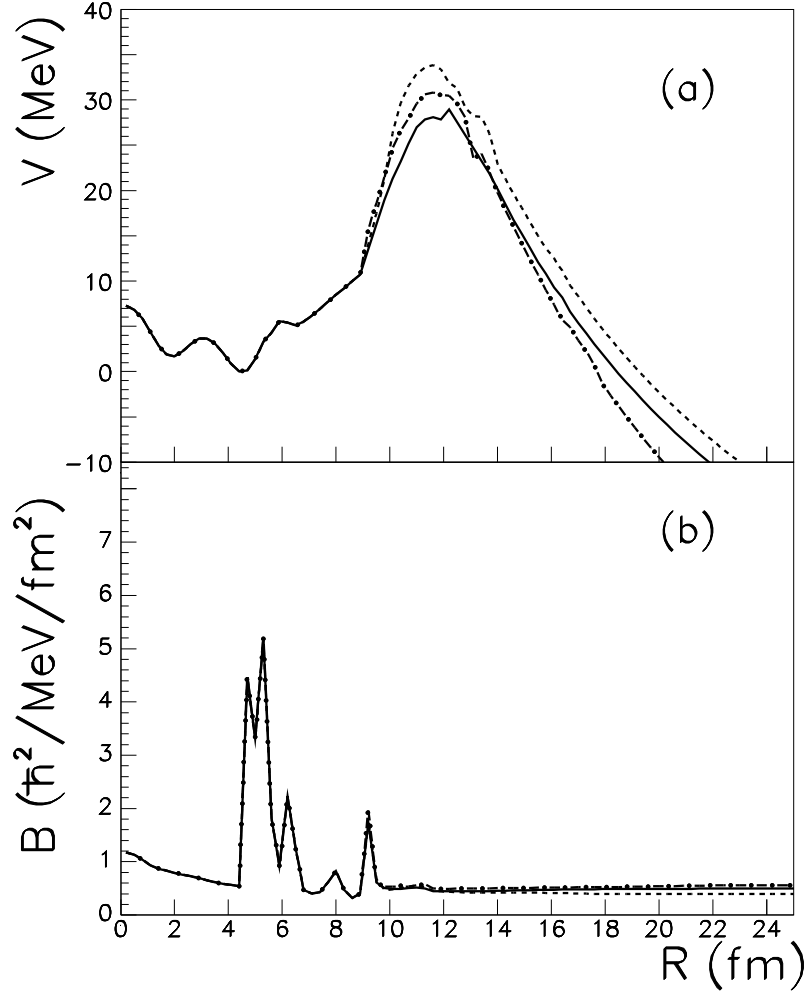


Figure 11: (a) Theoretical potential barriers  $V$  for the  $^{24}\text{Ne}$  emission (thick curve), for the  $^{28}\text{Mg}$  emission (dot-dashed curve) and  $^{22}\text{Ne}$  emission (dashed curve) as function of the elongation  $R$ . (b) The GOA effective mass along the minimal action trajectory for the three processes. The same line types are used as in panel (a).

In the proton diagram of Fig. 8, a decrease of the single particle energies after the scission can be observed due to the Coulomb mutual polarization. The energy slope for the light fragment is very large.

### 3.3. Half-life of $^{24}\text{Ne}$ emission from $^{232}\text{U}$

The shells corrections are displayed in Fig. 9. Notice that beyond  $R \approx 6$  fm, the total shell effect monotonically decreases up to the asymptotic final value. *Thus, the nucleus feels the existence of the  $^{208}\text{Pb}$  magic numbers in the overlapping region, well before scission.* The macroscopic-microscopic potential is plotted in Fig. 3(a) by a full line. The ground state is located at  $R \approx 4.6$  fm. Due to shells effects, a small pocket occurs in the barrier at  $R \approx 6.5\text{--}7$  fm. According to Fig. 2, at this elongation the emitted nucleus starts its preformation, that is the shape becomes necked in the median region of the nuclear shape. Therefore, this pocket occurs as a result of the shell effects of nascent fragments. Beyond this point, the increasing influence of the liquid drop barrier attenuates the microscopic effects. The liquid drop energy is plotted by a dashed line. The Coulomb interaction corrected to the experimental  $Q$ -value, i.e. the phenomenological quantity  $V_{\text{COU}} = Z_1 Z_2 / R - Q$  is also plotted in order to test the validity of the model. The theoretical and the phenomenological values agree well enough in the external part of the barrier, the difference being less than 2 MeV. This value agree with the r.m.s. deviations of the macroscopic-microscopic model [25]. In Fig. 9(b) the effective mass along the minimal action trajectory is plotted for the three mentioned models: cranking, GOA and CTDPE. The three inertia exhibit a similar shell structure. The cranking model gives the larger values, the GOA the smaller ones, while the CTDPE has always intermediate values. The variations of the inertia are mainly generated by the slope variation of the generalized coordinates.

The half-life of  $^{24}\text{Ne}$  emission was estimated by using a semi-empirical formula  $T_{1/2} = 0.72 \times 10^{-21} P^{-1}$  [s]. We used the three models for the inertia. The values of  $\log(T_{1/2}[\text{s}])$  are 35.66, 22.41 and 29.48. They were obtained for cranking model, the GOA and the CTDPE, respectively. The experimental value is 21.06. Thus, a reasonable agreement, less than two orders of magnitude, is obtained when the inertia is calculated within the GOA.

### 3.4. Predictions

We used this model to predict the best candidates for the cluster emission process from  $^{234}\text{U}$ . In order to follow the potential valley, the same trajectory was used up to an elongation  $R \approx 8$  fm and from this point the mass asymmetry was gradually changed to reach different final configurations. The barriers and the effective masses for the selected reactions are displayed in

Table 1: Logarithm of the cluster-decay half-lives from  $^{232}\text{U}$ . The first column indicates the emitted fragment, the second column gives the  $Q$ -value, the third column gives the experimental values, the fourth column gives the calculated half-lives within GOA effective masses. while the fifth column gives the phenomenological values.

Emitted nucleus	$Q$ -value (MeV)	$\log(T[\text{s}])$ Experimental [38]	$\log(T[\text{s}])$ Microscopic GOA	$\log(T[\text{s}])$ Phenomenological [39]
$^{24}\text{Ne}$	62.31	21.06	22.41	20.40
$^{28}\text{Mg}$	74.32		23.13	24.50
$^{22}\text{Ne}$	57.37		25.84	26.70

Fig. 11. The barriers for  $^{28}\text{Mg}$  and  $^{22}\text{Ne}$  emissions are larger than those obtained for  $^{24}\text{Ne}$ . Thus, the magnitude of the shell effects is larger when the daughter is the  $^{208}\text{Pb}$  double magic nucleus. The inertia along the least action trajectory is plotted in panel (b). The effective masses show similar shell structures, asymptotically reaching their appropriate reduced masses. Predictions concerning cluster decays from  $^{234}\text{U}$  are given in table 1. The microscopic results are compared to the experimental data [38] and with the those given by the analytical superasymmetric fission model [39], where the penetrabilities are obtained by using a phenomenological correction of the liquid drop external barrier taking into account the experimental  $Q$ -value of each process. Both theoretical estimations agree within one or two orders of magnitude.

#### 4. Conclusions

In this paper, the cluster decay was considered as a superasymmetric fission process and it was treated within the macroscopic-microscopic approximation. The fragmentation potential in the overlap region was obtained in conjunction with the minimal action principle. It was shown that the cluster decay follows a well behaved valley in the potential energy landscape, connected to the formation of the  $^{208}\text{Pb}$ . A pocket in the potential, due to large shell effects of the nascent  $^{238}\text{Pb}$ , was evidenced. This minimum is canceled by a rapid increase of the macroscopic barrier. *This behavior is very different with respect to the well known double humped fission barrier, where the second minimum occurs as a result of the strong shell effects in a*

*isomeric state of the parent nucleus.* These results give a better understanding of the cluster decay phenomenon and represent a contribution towards an unitary treatment of fission and heavy ion emission. Usually, the cluster decay is treated by calculating a preformation probability, as in the alpha decay [7, 40]. By using GOA inertia, the calculated half-life for the  $^{24}\text{Ne}$  emission from  $^{232}\text{U}$  shows a very good agreement with respect to the experimental data. Microscopic predictions concerning different decay modes were also given.

## 5. Acknowledgement:

Work performed in the frame of the CNCSIS IDEI 512 project of the Romanian Ministry of Education and Research.

## Appendix A. Inertia

Formulas for the elements of the tensor of inertia are given in this Appendix. In the cranking approximation, the inertia associated to two generalized coordinates  $q_i$  and  $q_j$  is

$$M_{ij}(q_1, q_2, \dots, q_n) = \frac{2}{\hbar^2} \sum_{\nu, \mu} \frac{\langle \nu | \frac{\partial H}{\partial q_i} | \mu \rangle \langle \mu | \frac{\partial H}{\partial q_j} | \nu \rangle}{(E_\nu + E_\mu)^3} (u_\nu v_\mu + u_\mu v_\nu)^2 + P_{ij} \quad (\text{A.1})$$

where  $\nu$  and  $\mu$  denote the single particle wave functions,  $E_\nu$ ,  $u_\nu$  and  $v_\nu$  are the quasiparticle energy, the vacancy and occupation amplitudes of the state  $\nu$ , respectively, in the BCS approximation, and  $P_{ij}$  is a correction that depends on the variation of the pairing gap  $\Delta$  and of the Fermi energy  $\lambda$  as function of the deformation coordinates  $q_i$ . This correction amount up to 10 % of the total value of the inertia. The inertia  $B$  along a trajectory in the configuration space spanned by the generalized coordinates  $q_i$  ( $i = 1, n$ ) can be obtained within the formula

$$B = \sum_{i=1}^n \sum_{j=1}^n M_{ij} \frac{\partial q_i}{\partial R} \frac{\partial q_j}{\partial R} \quad (\text{A.2})$$

Two other different approximation are tested, namely, the Gaussian Overlap Approximation (GOA) and the diabatic Cranking formula obtained from the Time Dependent Pairing Equations (CTDPE).

In the generator coordinate method [41, 42, 43, 44] the GOA inertia must be calculated separately for proton and neutron working spaces:

$$M_{n(p)} = 2\hbar^2 \frac{\left[ \sum_{\nu,\mu} P_{\nu\mu} P_{\mu\nu} (u_\nu v_\mu + u_\mu v_\nu)^2 \right]^2}{\sum_{\nu,\mu} (E_\nu + E_\mu) P_{\nu\mu} P_{\mu\nu} (u_\nu v_\mu + u_\mu v_\nu)^2} \quad (\text{A.3})$$

The quantities  $P_{\nu\mu}$  are given by the next formula that depends on a specific trajectory in the collective configuration space

$$P_{\nu\mu} = \sum_i^n P_{\nu\mu}(q_i) \frac{\partial q_i}{\partial R} \quad (\text{A.4})$$

where [42]

$$P_{\nu\mu}(q_i) = - \langle \nu | \frac{\partial H}{\partial q_i} | \mu \rangle \frac{u_\nu v_\mu + u_\mu v_\nu}{E_\mu + E_\nu} + \delta_{\nu\mu} \frac{\Delta}{2E_\nu^2} \left( \frac{\partial \lambda}{\partial q_i} + \frac{\epsilon_\nu - \lambda}{\Delta} \frac{\partial \Delta}{\partial q_i} \right) \quad (\text{A.5})$$

Here,  $\epsilon_\nu$  is the single particle energy of the state  $\nu$ . The inertia along a trajectory is given by the relation

$$B = \frac{(\gamma_n + \gamma_p)^2 M_n M_p}{\gamma_n^2 M_n + \gamma_p^2 M_p} \quad (\text{A.6})$$

where the index  $n$  stands for the neutrons while the index  $p$  is for protons. Moreover,  $\gamma$  is computed separately for protons and neutrons

$$\gamma = \sum_{\nu,\mu} P_{\nu\mu} P_{\mu\nu} (u_\nu v_\mu + u_\mu v_\nu)^2 \quad (\text{A.7})$$

In the case of the CTDPE [28] semi-adiabatic cranking model, the elements of the tensor of inertia are:

$$M_{ij} = 2\hbar^2 \sum_{\nu \neq \mu} \frac{(E_{\nu\mu} - E_0) \left( \frac{|\kappa_\nu \sqrt{\rho_\nu} \kappa_\mu|}{|\kappa_\nu| \sqrt{\rho_\mu}} - \frac{\kappa_\mu \sqrt{\rho_\mu} |\kappa_\nu|}{|\kappa_\mu| \sqrt{\rho_\nu}^2} \right) \langle \mu | \frac{\partial H}{\partial q_i} | \nu \rangle \langle \nu | \frac{\partial H}{\partial q_j} | \mu \rangle}{(E_{\nu\mu} - \sum_{\gamma \neq \nu,\mu} T_\gamma^{\nu\mu} - E_0 + \sum_\gamma T_\gamma)^2} \quad (\text{A.8})$$

where  $\kappa_\nu = u_\nu v_\nu$  is the pairing moment component,  $\rho_\nu = v_\nu^2$  is the occupation probability of the level  $\nu$  in the seniority zero state. The energies are of the seniority two states are:

$$E_{\nu\mu} = \sum_{\gamma \neq \nu,\mu} \rho_\gamma^{\nu\mu} \epsilon_\gamma - \frac{|\Delta_{\nu\mu}|^2}{G} - G \sum_{\gamma \neq \nu,\mu} (\rho_\gamma^{\nu\mu})^2 + \epsilon_\nu + \epsilon_\mu \quad (\text{A.9})$$

where the levels  $\epsilon_\nu$  and  $\epsilon_\mu$  are blocked, the values of  $\rho_\gamma^{\nu\mu}$  address occupation probabilities for the seniority two states and

$$T_\gamma^{\nu\mu} = 2\rho_\gamma^{\nu\mu}\epsilon_\gamma - 2G(\rho_\gamma^{\nu\mu})^2 + \frac{\kappa_\gamma^{\nu\mu}\Delta_{\nu\mu}^* + (\kappa_\gamma^{\nu\mu})^*\Delta_{\nu\mu}}{2} \left( \frac{(\rho_\gamma^{\nu\mu})^2}{|\kappa_\gamma^{\nu\mu}|^2} - 1 \right) \quad (\text{A.10})$$

The energy  $E_0$  is the seniority zero state. All quantities without both indexes  $\nu\mu$  address the seniority zero state. The inertia along the trajectory is obtained within Rel.(A.6). The final value of  $B$  is a sum of the quantities obtained for protons and neutrons as in the classical cranking model.

A comparison between the behavior given by these three approximations concerning the fission can be found in Ref. [45].

## References

- [1] A. Sandulescu, W. Greiner, J. Phys. G 3 (1977) L189.
- [2] A. Sandulescu, H.J. Lustig, J. Hahn, W. Greiner, J. Phys. G 4 (1978) L279.
- [3] A. Sandulescu, D.N. Poenaru, W. Greiner, Sov. J. Part. Nucl. 11 (1980) 528.
- [4] A. Sandulescu, J. Phys. G 15 (1989) 529.
- [5] A. Sandulescu, W. Greiner, Rep. Prog. Phys. 55 (1992) 1423.
- [6] A. Sandulescu, D.N. Poenaru, W. Greiner, J.H. Hamilton, Phys. Rev. Lett. 54 (1985) 490.
- [7] D.S. Delion, *Theory of particle and cluster emission*, Springer-Verlag, Berlin (2010).
- [8] H.J. Rose, G.A. Jones, Nature 307 (1984) 245.
- [9] E. Hourani, M. Hussonois, L. Stab, et al., Phys. Lett. B 160 (1985) 375.
- [10] S. Gales, E. Hourani, M. Hussonois, H.P. Shapira, M. Vergnes, Phys. Rev. Lett. 53 (1984) 759.
- [11] S.W. Barwick, P.B. Price, J.D. Stevenson, Phys. Rev. C 31 (1984) 1984.

- [12] M. Greiner, W. Scheid, J. Phys. G 12 (1986) 229 .
- [13] L. Brillard, A.G. Elayi, E. Hourani, M. Hussonnois, J.F. Le Du, L.H. Rosier, L. Stab, C.R. Acad. Sci. Ser. II 309 (1989) 1105.
- [14] M. Hussonnois, J.F. Le Du, L. Brillard, J. Dalmaso, G. Ardisson, Phys. Rev. C 43 (1991) 2599.
- [15] M. Mirea, Phys. Rev. C 57 (1998) 2484.
- [16] M. Mirea, Phys. Rev. C 78 (2008) 044618 .
- [17] J.R. Nix, Ann. Rev. Nucl. Sci. 20 (1972) 65.
- [18] M. Mirea, L. Tassan-Got, Cent. Eur. J. Phys. 9 (2011) 116.
- [19] M. Mirea, Phys. Lett. B 680 (2009) 316.
- [20] M. Mirea, D.S. Delion, A. Sandulescu, Phys. Rev. C 81 (2010) 044317.
- [21] M. Brack, J. Damgaard, A.S. Jensen, H.C. Pauli, V. M. Strutinsky, Rev. Mod. Phys. 44 (1972) 320.
- [22] K.T.R. Davies, J.R. Nix, Phys. Rev. C 14 (1976) 1977.
- [23] D.N. Poenaru, M. Ivascu, D. Mazilu, Comp. Phys. Commun. 19 (1980) 205.
- [24] M. Mirea, O. Bajeat, F. Clapier, F. Ibrahim, A.C. Mueller, N. Pauwels, J. Proust, Eur. Phys. J. A 11 (2011) 59.
- [25] P. Moller, J.R. Nix, W.D. Myers, W.J. Swiatecki, At. Data and Nucl. Data Tabl. 59 (1995) 185.
- [26] D.N. Poenaru, D. Mazilu, M. Ivascu, J. Phys. G 5 (1979) 1093.
- [27] M. Mirea, Phys. Rev. C 83 (2011) 054608.
- [28] M. Mirea, R.C. Bobulescu, J. Phys. G 37 (2010) 055106.
- [29] M. Mirea, Nucl. Phys. A 780 (2006) 13.
- [30] M. Mirea, Phys. Rev. C 54 (1996) 302.

- [31] M. Mirea, Phys. Rev. C 63 (2001) 034603.
- [32] M. Mirea, Eur. Phys. J. A 4 (1999) 335.
- [33] P. Stoica, Rom. Rep. Phys. 63 (2011) 76.
- [34] M. Mirea, D.S. Delion, A. Sandulescu, EPL 85 (2009) 12001.
- [35] M. Mirea, A. Sandulescu, D.S. Delion, Proc. Rom. Acad. in print (2011).
- [36] D.N. Poenaru, M. Mirea, W. Greiner, I. Cata, D. Mazilu, Mod. Phys. Lett. A 5 (1990) 2101.
- [37] M. Mirea, L. Tassan-Got, C. Stephan, C.O. Bacri, Nucl. Phys. A 735 (2004) 21.
- [38] S.W. Barwick, P.B. Price and J.D. Stevenson, Phys. Rev. C 31 (1985) 1984.
- [39] D.N. Poenaru, W. Greiner, K. Depta, M. Ivascu, D. Mazilu, and A. Sandulescu, At. Data Nucl. Data Tables 34 (1986) 423.
- [40] R.G. Lovas, R.J. Liotta, A. Insolia, K. Varga, D.S. Delion, Phys. Rep. 294 (1989) 265.
- [41] S.J. Wang, W. Cassing and W. Norenberg, Phys. Lett. B 131 (1983) 265.
- [42] C. Fiolhais, and R.M. Dreizler, Nucl. Phys. A 393 (1983) 205.
- [43] A. Gozdz, K. Pomorski, M. Brack and E. Werner, Nucl. Phys. A 442 (1985) 26.
- [44] A. Gozdz, K. Pomorski, M. Brack and E. Werner, Nucl. Phys. A 442 (1985) 50.
- [45] M. Mirea, Rom. Rep. Phys. in print (2011).